PNAS RESEARCH ARTICLE | APPLIED PHYSICAL SCIENCES

On the shape of air bubbles trapped in ice

Virgile Thiévenaz[a,b,1], Jochem G. Meijer[c], Detlef Lohse[c,d], and Alban Sauret[b,e]

Edited by Pablo Debenedetti, Princeton University, Princeton, NJ; received July 29, 2024; accepted January 10, 2025

Water usually contains dissolved gases, and because freezing is a purifying process these gases must be expelled for ice to form. Bubbles appear at the freezing front and are then trapped in ice, making pores. These pores come in a range of sizes from microns to millimeters and their shapes are peculiar; never spherical but elongated, and usually fore-aft asymmetric. We show that these remarkable shapes result of a delicate balance between freezing, capillarity, and mass diffusion. A nonlinear ordinary differential equation suffices to describe the bubbles, which features two nondimensional numbers representing the supersaturation and the freezing rate, and two additional parameters representing simultaneous freezing and nucleation treated as the initial condition. Our experiments provide us with a large variety of pictures of bubble shapes. We show that all of these bubbles have their rounded tip well described by an asymptotic regime of the differential equation and that most bubbles can have their full shape quantitatively matched by a full solution. This method enables the measurement of the freezing conditions of ice samples, and the design of freeze-cast porous materials. Furthermore, the equation exhibits a bifurcation that explains why some bubbles grow indefinitely and make long cylindrical "ice worms," well known to glaciologists.

ice | bubbles | freeze-casting | capillarity | bifurcation

Significance

Freezing a gas-laden liquid makes a porous solid. By studying the size and shape distribution of pores in ice, glaciologists can infer its conditions of formation. Conversely, material scientists can produce porous media by "freeze-casting" a liquid, for example molten metal, in which gas is dissolved. In both cases, the challenge is to link the pore size and shape distributions, observed or desired, to the gas concentration and the freezing rate. Pushing beyond empirical studies, we propose an analytical model to describe the growth of the pores which explains the distinct features of their shape.

Ice frozen from water containing dissolved air is usually not clear but opaque, because it includes many bubbles (1). This is commonly observable in ice cubes from a freezer. These bubbles have peculiar shapes, never spherical but elongated (Fig. 1). Some even reach lengths of several centimeters (2)—they are named "ice worms" (3) or "worm bubbles" (4). Gases are soluble in liquid water but not in ice, so that when water freezes the dissolved gases are expelled and concentrate in the liquid (5). Bubbles eventually nucleate near the freezing front and are captured by ice, while at the same time they keep growing by diffusion of the gas. Ice thus formed is porous. Usually, one speaks of bubbles in water and pores in ice.

In the natural environment, porous ice is the rule rather than the exception. Hailstones (6) and lake ice (4, 7) contain pores made out of the dissolved gas. Glacier ice is also porous but is made out of compacted snow and not frozen gas-laden water (8). In winter, sap freezes inside plants and bubbles form; after the thaw, these bubbles may prevent the flow of sap (winter embolism) (9). Generally, freeze-thaw cycles can dramatically affect the stability of complex media, like food (10), and the survival of living organism (11, 12).

In addition to water, gases are soluble in a large variety of liquids, including metals (13), silica (14) and sapphire (15, 16); freezing such gas solutions yields porous materials. Porosity is usually a defect of which to get rid (17, 18). However, for certain applications, porosity is desired and therefore the size and shape of the pores must be controlled (19). More generally, the freezing of solutions of gases or other solutes makes various freeze-cast materials (20–22), some of which are biocompatible (23). During the freezing of a suspension or of an emulsion, the dispersed particles may or may not be engulfed in ice, depending on the freezing rate (24). Their engulfment deforms the freezing front (25), according to their thermal properties (26). The particles themselves may deform when they are captured; for example, oil droplets in an emulsion make pointy oil drops in ice (27, 28).

Several attempts at describing the growth and entrapment of gas bubbles have been made, either using scaling laws (29), or taking into account the numerous mechanisms at play (heat transfer, phase change, capillarity, mass diffusion, nucleation) (5, 30, 31). Freezing and capillarity make a challenging combination. For example, a sessile drop freezing will grow a tip (32–35). Also, ice is actually not perfectly hydrophilic, so that water may retract on ice instead of spreading (36–38).

In this paper, we investigate the shape of the pores formed during the freezing of ice, and how it is set by the growth history of bubbles. We show that under certain

Author affiliations: [a]Physique et Mécanique des Milieux Hétérogènes, Centre Nationale de la Recherche Scientifique, École Supérieure de Physique et de Chimie Industrielles de la Ville de Paris, Sorbonne Université, Université Paris-Cité, Paris F-75005, France; [b]Department of Mechanical Engineering, University of California, Santa Barbara, CA 93106; [c]Department of Science and Technology, Physics of Fluids Group and Max Planck Center for Complex Fluid Dynamics, J.M. Burgers Center for Fluid Dynamics, University of Twente, Enschede 7500AE, The Netherlands; [d]Max Planck Institute for Dynamics and Self-Organization, Göttingen 37077, Germany; and [e]Department of Mechanical Engineering, University of Maryland, College Park, MD 20742

Author contributions: V.T., J.G.M., D.L., and A.S. designed research; V.T. and J.G.M. performed research; V.T. and J.G.M. analyzed data; V.T. performed mathematical analysis; and V.T., D.L., and A.S. wrote the paper.

The authors declare no competing interest.

This article is a PNAS Direct Submission.

[1]To whom correspondence may be addressed. Email: virgile.thievenaz@espci.fr.

This article contains supporting information online at https://www.pnas.org/lookup/suppl/doi:10.1073/pnas.2415027122/-/DCSupplemental.

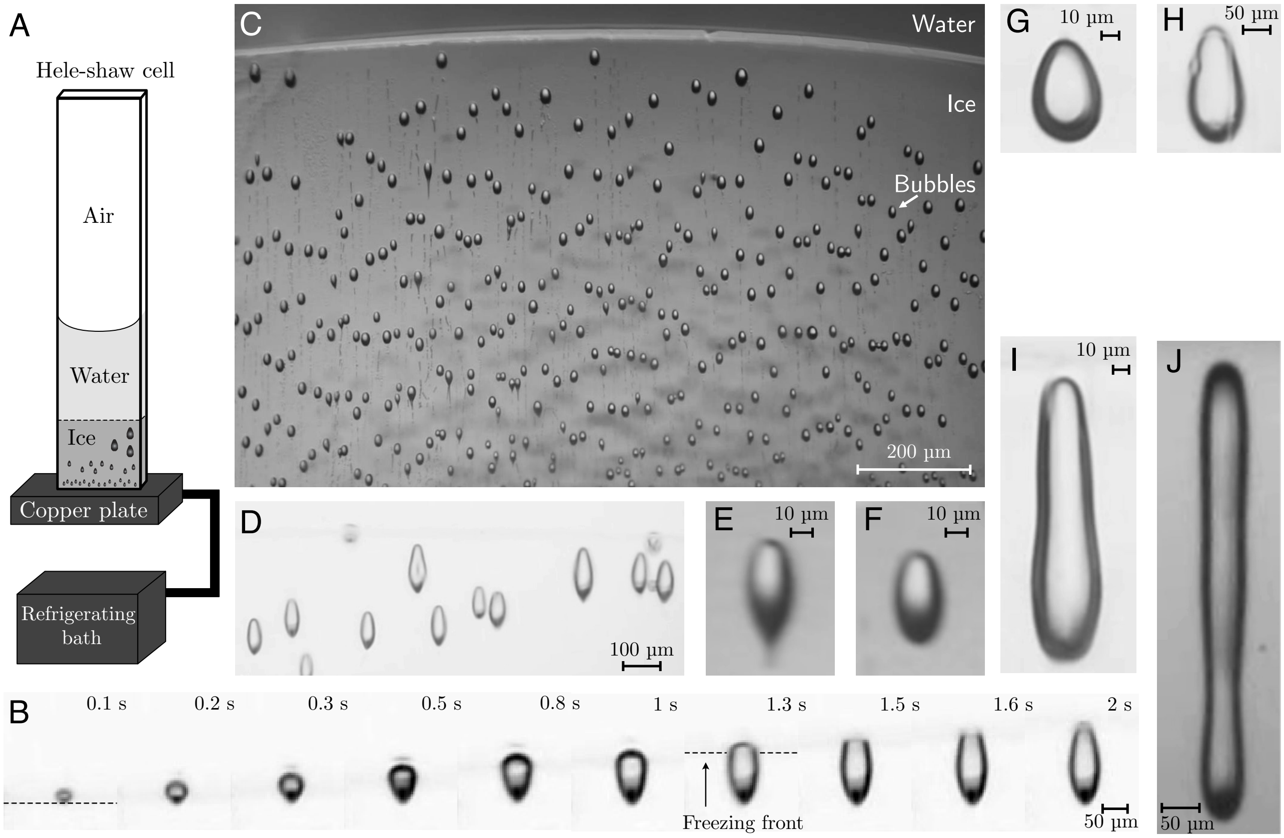

Fig. 1. (*A*) Schematic of the experimental setup. (*B*) Timelapse of the nucleation, entrapment, growth, and closure of a gas bubble at the ice–water interface, for a freezing rate of 54 μm/s. (*C*) Small pores in ice frozen at 133 μm/s. (*D*) Long pores in ice frozen at 46 μm/s. Other pictures describe particular cases: (*E*) $v = 91$ μm/s, with nucleation between ice grains; (*F*) $v = 90$ μm/s, with nucleation at the freezing front; (*G*) $v = 21$ μm/s, with nucleation 35 μm away from the freezing front; (*H*) $v = 20$ μm/s, with nucleation 100 μm away from the freezing front; (*I*) short ice worm for $v = 13$ μm/s; and (*J*) Worm bubble from second experimental setup (*Materials and Methods*).

assumptions, this problem reduces to a single nonlinear ordinary differential equation, which we study analytically. Two asymptotic regimes are found, one corresponding to fast freezing and the other to the closing of the bubble. Under a certain freezing velocity the system undergoes a bifurcation, after which bubbles do not close any more, thus explaining how worm bubbles appear and what their equilibrium radius is. Our equation can also be solved numerically, and its solutions matched to the shapes of pores obtained experimentally by freezing deionized water at various freezing rates. In most cases, a quantitative agreement is found between the solution and the experiments.

Experiments

Much work having already been dedicated to describing the pores in ice (2, 5, 6, 29–31, 39), the main purpose of our experiments is to provide a basis of comparison with our model, as well as a qualitative description for the reader to better understand the problem and the assumptions of the model.

We study the freezing of water, in which gases are naturally dissolved, in a Hele-Shaw cell for freezing rates varying between 12 μm/s and 263 μm/s (Fig. 1*A* and *Materials and Methods*). Fig. 1*B* reports the formation of a pore at a freezing rate of 54 μm/s. First, a bubble nucleates at the freezing front. Then, this bubble grows by diffusion of dissolved gas, while the freezing front keeps advancing. The bubble expands radially up to a maximum after which it shrinks. Eventually, the freezing front passes by and the pore closes; its final shape is set. For the case shown in Fig. 1*B*, the whole process takes about 2 s, and the final bubble is 154 μm-long and 64 μm-wide.

The pores in ice are never spherical, but elongated in the direction of freezing. Their number also varies with the freezing rate. At a high freezing rate (Fig. 1*C*, 133 μm/s on average), many small pores, slightly elongated, are formed. Conversely, at a slower freezing rate (Fig. 1*D*, 46 μm/s), fewer pores are formed, and they are bigger and longer.

The place of nucleation of the bubble and the time elapsed before it is trapped may also influence greatly its final shape. For fast freezing (about 90 μm/s) the bubble may (Fig. 1*E*) or may not (Fig. 1*F*) show a "tail." This likely corresponds to whether or not the bubble was trapped by a single ice crystal or at the junction of two crystals, i.e. at a grain boundary. In the latter case, the initial growth of the bubble is restrained between two crystals, and this gives it the tail.

Although nucleation usually occurs at the freezing front, we observe some cases in which the bubble nucleates ahead of the front, probably on some tiny impurity (see Fig. 1 *G* and *H* and the corresponding videos) (40). For slow freezing, the distance between the nucleation point and the freezing front matters greatly because it sets the time span during which the bubble may grow before being trapped. For instance, the pores shown in Fig. 1 *G* and *H* grew and froze under the same freezing rate of 20 μm/s; however, their shapes are different. The former is 53 μm-long and 36 μm-wide, whereas the latter is 200 μm-long and 96 μm-wide; its aspect ratio is larger. The difference is that the corresponding bubbles nucleated 35 μm away from the freezing front (Fig. 1*G*), and 100 µm away from it (Fig. 1*H*). The latter had about 3 s more to grow freely, eventually yielding a different shape, not only a different size. This observation reveals the strong dependence of the bubble shape on the initial bubble size.

The nucleation of gas bubbles in water is quite complex because of the chemistry it involves (41). In the following, we shall focus on the growth of the bubble at the freezing front, after the nucleation and the trapping. As we shall show, the growth can be well described by a single ordinary differential equation. Nucleation and entrapment will appear as initial conditions.

Our first experimental setup, from which the pictures of Fig. 1 *A–I* and most of our experimental data were obtained, could not maintain freezing rates slower than 12 µm/s with sufficient stability. The fluctuations of the freezing rate in this system are indeed of the order of a few µm/s. We studied worm bubbles using another experimental setup, described in *Material and Methods*. This second system enabled us to vary the freezing rates between 4 µm/s and 17 µm/s with a stability of the order of a few tenths of µm/s. We used this setup to generate worm bubbles (Fig. 1*J*).

The Frozen Bubble Equation

Our model is based on the conservation of the mass of gas. For simplicity, we treat air as a simple gas and average its properties over that of nitrogen and oxygen (*Material and Methods*). During its growth, the bubble can be separated into two parts: a *Lower* part, the pore, that is trapped in the ice, and an *Upper* part, the bubble per se, that is in contact with the liquid water (Fig. 2). As water freezes, gas is virtually transferred from the bubble to the pore. In the meantime, gas may be exchanged between the bubble and the surrounding water. The direction and magnitude of this mass transfer depends on the Laplace pressure, hence on the curvature of the bubble.

The shape of the ice–water interface results of the balance between latent heat and the heat fluxes on either side. Since the heat conductivity of gas is negligible compared to that of water and ice, the heat flux toward the bubble $\boldsymbol{J}_{\mathrm{g}}$ must be negligible as well, hence the streamlines of the heat flux must be tangent to the bubble. Being the isotherm corresponding to the freezing temperature, the freezing front should be orthogonal to the streamlines and therefore orthogonal to the bubble. Therefore, we will assume that the contact angle of the bubble on the ice is close to $\pi/2$, as observed for instance in the freezing of sessile drops (34, 35). The difference between the actual contact angle and $\pi/2$ (denoted ε in Fig. 2) will be neglected; this assumption is supported a posteriori by our measurements. Since the bubble is much smaller than the capillary length (2.7 mm for water), the liquid–gas interface has a uniform curvature; it is a spherical cap. In summary, heat transfer and capillarity impose that the upper part of the bubble be a hemisphere of radius R. Let R be the radius of that hemisphere, and also the radius of the contact line between the bubble and the freezing front. The rest of the model consists in writing an evolution equation for $R(t)$ and then in constructing the shape of the pore by translation of the contact line of radius $R(t)$ at velocity v.

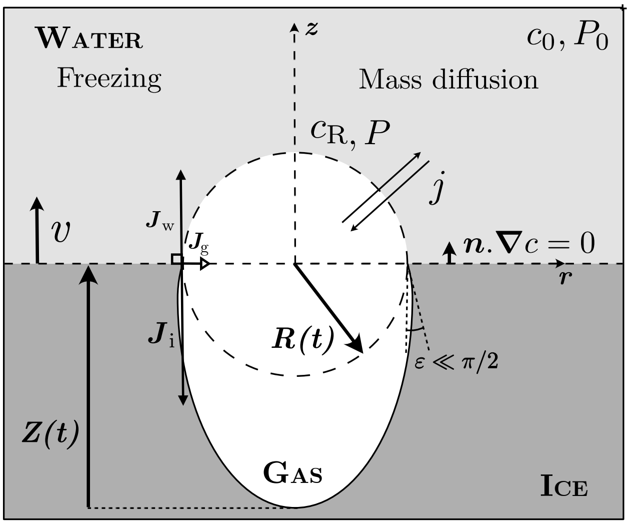

Fig. 2. Schematic of the model. The *Upper* part of the gas is the bubble, in contact with water; the *Lower* part is the pore, in contact with ice. On the *Left* thermal effects are shown, on the *Right* mass diffusion effects.

In order to simplify the calculations, we assume that the gas concentration far away from the bubble, $c(r \to \infty) = c_0$, is constant. In practice, gas is released into the liquid at the freezing front, and that creates a concentration profile in the z-direction with a strong gradient near the front. More specifically, $c(z)/c_0 \sim \exp\left(-z\,v/D\right)$ (6), with D the gas diffusivity. Meijer et al. have recently estimated the gradient on similar experiments (40); they find that it is of order 1 (mg/L)/mm. For the gas concentrations considered here, it means that the concentration profile near the front far from the bubble smoothes out over a length scale D/v, which is of order of 10 µm, about the size of the bubble. Furthermore, for not too slow v, gas accumulates at the front during the freezing process, so that for large pores frozen over a long time the surrounding gas concentration may increase in time. The physical meaning of c_0 is therefore closer to an effective concentration, which averages out the concentration gradients created by phenomena other than the growth of the current bubble.

The bubble grows out of the gas-saturated water by mass transfer. The corresponding mass flux can be expressed in a closed form by solving the diffusion equation in the half-space bounded by a plane upon which sits a hemisphere. Under the hypothesis that the boundary condition on the plane is that of zero normal flux, the problem reduces to the rotation-invariant problem of diffusion around sphere. In spherical coordinates this problem is written

$$\frac{D}{r^2}\frac{\partial}{\partial r}\left(r^2\frac{\partial c}{\partial r}\right) = \frac{\partial c}{\partial t}, \qquad [1]$$

$$c(t=0, r) = c_0, \qquad [2]$$

$$c(t, r=R) = c_{\mathrm{R}}, \qquad [3]$$

$$c(t, r \to \infty) = c_0, \qquad [4]$$

where c_0 and c_{R} denote the boundary conditions at infinity and at the bubble interface, respectively, and where $D = 2 \cdot 10^{-9}\,\mathrm{m}^2/\mathrm{s}$ is the diffusion coefficient of air in water (42). This problem was solved by Epstein and Plesset (43), and they obtained a closed form for the surface density of mass flux through the gas–water interface:

$$j = D(c_0 - c_{\mathrm{R}})\left(\frac{1}{R} + \frac{1}{\sqrt{\pi D t}}\right). \qquad [5]$$

The origin of times in Eq. **5** corresponds to when diffusion starts, that is when the bubble nucleates. The solution of the Epstein and Plesset equation is applicable for a bubble in an infinite space. In our experiments, bubbles are "confined" for easier visualization, but the gap between the glass slides is at least ten times bigger than the bubbles, so the Epstein and Plesset equation is still approximately applicable.

Far from the bubble, water is at ambient pressure P_0, and gas is in excess by a quantity $\Delta c > 0$ with respect to the solubility: $c_0 = c_s(P_0) + \Delta c$. Hydrostatic pressure is negligible, given the height of the water column (a few centimeters) above the bubble. The solubility of gases in water c_s depends linearly on pressure through Henry's law: $c_s(P) = c_s(P_0) + k_H(P - P_0)$. The constant k_H for air is 2.95×10^{-5}kg.Pa^{-1}.m^{-3}, as calculated from the solubility of nitrogen and oxygen (42). At the gas–water interface, the Laplace pressure leads to an increase of the solubility: $c_R = c_s(P_0) + 2\gamma k_H/R$. $\gamma = 75$ mN/m is the surface tension of water at 0 °C. Therefore, the concentration gap between the interface and the surrounding water is

$$c_0 - c_R = \Delta c - 2k_H\gamma/R. \qquad [6]$$

We can now write the conservation of the mass of gas in the upper part of the bubble:

$$\frac{\mathrm{d}}{\mathrm{d}t}\left(\frac{2\pi}{3}\rho R^3\right) = 2\pi R^2 j - \pi R^2 \rho v. \qquad [7]$$

$\rho = 1.2$ kg/m^3 is the density of air. The density mismatch between water and ice is accounted for by the freezing rate v. Substituting the expression of the flux density j (Eqs. **5** and **6**) into the mass balance, and introducing $R_c = 2\gamma k_H/\Delta c$ we obtain

$$\frac{\mathrm{d}R}{\mathrm{d}t} = \frac{D\Delta c}{\rho R_c}\left(1 - \frac{R_c}{R}\right)\left(\frac{R_c}{R} + \frac{R_c}{\sqrt{\pi D t}}\right) - \frac{v}{2}. \qquad [8]$$

Let us define $Z(t)$ so that

$$\frac{\mathrm{d}Z}{\mathrm{d}t} = v, \qquad [9]$$

then $[Z(t), R(t)]$ is a parametric curve that describes the shape of the pore.

A direct consequence of Eq. **8** is that the bubble can only grow if $R > R_c$. This observation reveals the physical meaning of R_c: It is the critical radius a bubble must have to be stable against dissolution under Laplace pressure. Therefore, even if the water around the bubble is supersaturated with gas, the bubble may still dissolve if it is too small. The condition $R > R_c$ is nevertheless not sufficient to maintain stability, because freezing contributes negatively to $\frac{\mathrm{d}R}{\mathrm{d}t}$.

In the rest of the paper, we shall restrict ourselves to the case of constant freezing rate ($\frac{\mathrm{d}v}{\mathrm{d}t} = 0$). Not only does this simplify greatly the analysis, it also corresponds to our experimental situation. Therefore, Eq. **9** becomes trivial and its solution $Z = vt$ can be combined with Eq. **8** to reduce the problem to a single nonlinear ordinary differential equation. We write this equation in nondimensional form by taking R_c as unit length and R_c^2/D as unit time:

$$\frac{\mathrm{d}R}{\mathrm{d}Z} = \frac{\delta}{\zeta}\left(1 - \frac{1}{R}\right)\left(\frac{1}{R} + \sqrt{\frac{\zeta}{\pi Z}}\right) - \frac{1}{2}. \qquad [10]$$

We refer to Eq. **10** as the Frozen Bubble Equation. It has two nondimensional parameters: $\delta = \Delta c/\rho$ is the nondimensional supersaturation, and $\zeta = vR_c/D$ is the ratio of the characteristic times of freezing and mass diffusion. In the following, we denote $R' = \frac{\mathrm{d}R}{\mathrm{d}Z}$.

Analysis

The Fast Freezing Regime ($\zeta \gg \delta$). Before turning to the general analysis of the Frozen Bubble Equation, we describe the specific case in which mass diffusion is negligible compared to freezing. Taking $\zeta \to \infty$, Eq. **10** reduces to $R' = -1/2$. The upper part of the pore then has the shape of a cone of angle $\theta_c = \arctan(1/2) \simeq 26.5°$ (Fig. 3*A*). For finite $\zeta \gg \delta$, we solve the Frozen Bubble Equation numerically to check that the shapes of the pores indeed converge toward a conical tip.

Taking the limit $\zeta \to \infty$ amounts to canceling the possibility of gas transfer between the bubble and the liquid, meaning the two substances are immiscible. It is interesting to note that in this limit case, the volume of the cone must be that of a hemisphere of radius R, so the mass of gas is conserved. Satisfying this condition requires that the height of the cone be equal to its maximal diameter, a condition strictly equivalent to $\theta_c = \arctan(1/2)$. Therefore, in the absence of heat and mass transfer between the bubble and the liquid, the final pore has the shape of a cone on top of a hemisphere, and its aspect ratio is 3/2. This shape is quite similar to that of pointy oil drops in frozen emulsions (27, 28), although in that case there is no reason to assume a 90° contact angle between oil and the freezing front.

The Limit $R \to 0$ and the Tip of the Pore. Another interesting regime is the limit $R \to 0$. It corresponds to the closing of the pore. Taking $R \ll 1$ in the Frozen Bubble Eq. **10**, we obtain

$$\frac{\mathrm{d}R}{\mathrm{d}Z} = -\frac{\delta}{\zeta}\frac{1}{R^2}, \qquad [11]$$

which is readily integrated near the closing point of the bubble $R(Z_{\max}) = 0$. Near the tip the pore shape should therefore follow:

$$R(Z) = \left(\frac{3\delta}{\zeta}(Z_{\max} - Z)\right)^{1/3}. \qquad [12]$$

This asymptotic regime is observed approximately in all our experiments. Fig. 3*B* shows a selection of pore profiles extracted from experiments, representative of the whole range of freezing rates, rescaled according to Eq. **12**. For all pores we obtain a good

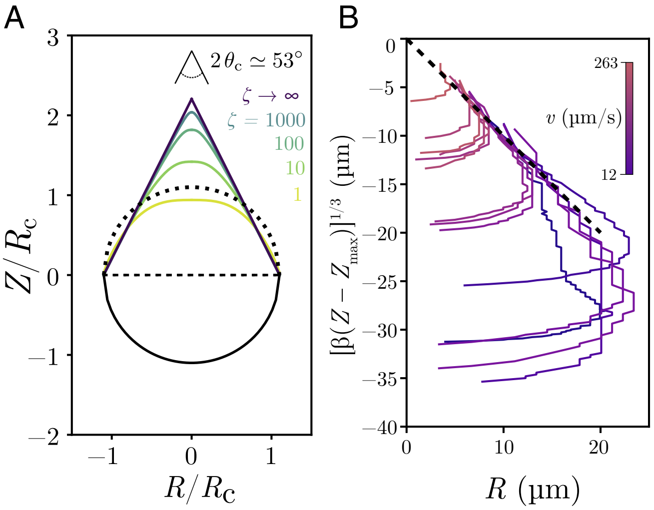

Fig. 3. (*A*) Solutions of Eq. **10** in the limit $\zeta \gg \delta$, for $\delta = 1$ and various values of ζ. The case $\zeta \to \infty$ is the analytical solution. (*B*) Rescaling of the shape of the pores near the tip according to Eq. **12**. The prefactor β is fitted for each profile. The dashed line has slope −1.

agreement with Eq. **12**, which in dimensional form is written $R = \left[\beta\left(Z_{\max} - Z\right)\right]^{1/3}$ with $\beta = 3\delta R_c^2/\zeta$. It is notable that β does not depend on Δc. The closing of the pore proceeds regardless of the supersaturation, only driven by the Laplace pressure. Below (*Shape Matching*), we overlay the cubic shape described by Eq. **12** onto the profiles.

Alternative form of the Frozen Bubble Equation. The set of values for parameters δ and ζ supplemented with an initial condition $R_0 = R(Z_0)$ makes a unique solution of Eq. **10**. To compare solutions to experimental pores, it is more practical to introduce the initial slope $R'(Z_0) = R'_0$, and to express the ratio δ/ζ as a function of the four parameters R_0, Z_0, R'_0, and ζ. Eq. **10** can thus be recast in an elegantly symmetric form:

$$\frac{R'(Z) + \frac{1}{2}}{R'_0 + \frac{1}{2}} = \frac{1 - \frac{1}{R}}{1 - \frac{1}{R_0}} \times \frac{\frac{1}{R} + \sqrt{\frac{\zeta}{\pi Z}}}{\frac{1}{R_0} + \sqrt{\frac{\zeta}{\pi Z_0}}}. \qquad [13]$$

R_0, Z_0, and R'_0 are geometrical quantities that can be measured experimentally.

The Bifurcation at $\delta = 2\zeta$ and Bubbles that Never Close. The general analysis of the solutions of the nonlinear Frozen Bubble Equation can be performed using geometrical techniques. In the (Z, R)-plane, Eq. **10** defines a vector field; at point (Z, R) the vector orientation is $R'(Z)$ (44). Starting with the initial condition $R(Z_0) = R_0$, the solution is then the curve that passes through (Z_0, R_0) and is everywhere tangent to a vector of the field. An example is shown in Fig. 4*A* for $\delta = 1$ and $\zeta = 0.7$. The dashed blue curve is the separatrix between two domains. On the left, $R' > 0$ so the bubble grows; on the right, $R' < 0$ so the bubble shrinks. Starting from different initial conditions, the bubble will grow for some time before it shrinks, or it will shrink right from the start without growing.

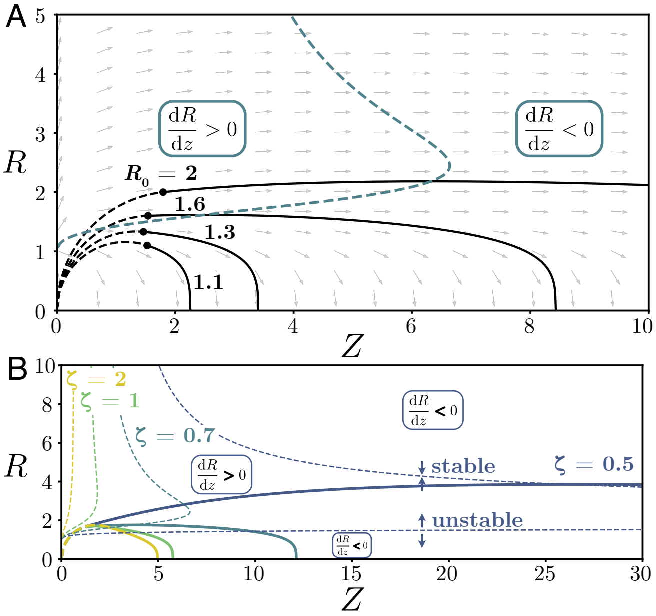

Fig. 4. (*A*) Vector field associated with Eq. **10** for $\delta = 1$ and $\zeta = 0.7$. It draws a phase space with domains where the bubble grows ($R' > 0$, *Left*) and shrinks ($R' < 0$, *Right*). The blue dashed line is the separatrix between the domains. The black points represent different initial conditions continued to the right into solutions (solid lines). The dashed curves represent a spherical shape that matches the initial condition. (*B*) Evolution of the phase space and the separatrix with decreasing ζ for constant $\delta = 1$.

Taking $R' = 0$ in Eq. **10**, we find the equation of the separatrix:

$$Z = \frac{\zeta}{\pi}\left(\frac{R\,(R-1)}{\left(\frac{\zeta}{2\delta}\right) R^2 - R + 1}\right)^2. \qquad [14]$$

The relevant properties of the phase space associated to Eq. **10** are the number and the shape of the domains in which the slope R' keeps a constant sign. For $\delta < 2\zeta$, the separatrix is bounded on the Z-axis and the domain to its right corresponds to $R' < 0$ (Fig. 4*B*). Therefore, after some possible growth depending on the initial condition, the bubble must shrink and close. At $\delta = 2\zeta$ there is a bifurcation: The extent of the separatrix on the Z-axis diverges. For $\delta > 2\zeta$, the function $Z(R)$ defined by Eq. **14** has two real poles at

$$R_{\pm} = \frac{\delta}{\zeta} \pm \sqrt{\frac{\delta}{\zeta} - 2}, \qquad [15]$$

corresponding to two disjoint branches of the separatrix. Above the lower branch $R' > 0$ and below it $R' < 0$, therefore it is unstable. However, the upper branch is stable. If the initial condition is above the lower branch ($R_0 > R_-$), the bubble will grow until it is captured by the upper branch, and it will never close, making a worm bubble of equilibrium radius R_+ (Fig. 4*B*).

In reality, worm bubbles have a finite length. Within the model, this would be possible if δ or ζ would fluctuate so much that the system would switch domains in Fig. 4*B*. Inverting Eq. **15** gives the typical size of the fluctuation of δ/ζ required to close the worm bubble of a certain radius. It is notable that the ratio δ/ζ scales like Δc^2. Minute variations of concentration may thus affect greatly the shape of the bubbles. Such variations could come from fluctuations of the freezing rate. It could also come from fluctuations of the gas concentration due to the nucleation and growth of other neighboring bubbles. Furthermore, pressure variations in the liquid during the growth are known to modulate the radius of worm bubbles (2). Such pressure variations could be taken into account in our model by modifying Eq. **6**.

Shape Matching

Closed Pores. Our experiments give us access to pictures of frozen bubbles of which we know at what rate they froze. Unknown are the supersaturation Δc around the bubble when it appears and the nucleation process. In the following, we match numerical solutions of the Frozen Bubble Equations to the pores observed in our experiments. For simplicity, we shall assume that nucleation and entrapment leave the bottom of the bubbles spherical—that is, of uniform curvature—up to the point (Z_0, R_0). Therefore, in Eq. **13** the initial slope can be expressed as $R'_0 = \left(R_0^2 - Z_0^2\right)/2R_0Z_0$. We measure Z_0 and R_0 on the profiles and fit R_c by matching the overall shape of the bubble; thence, we compute ζ, δ, and Δc.

After its shape is matched with a solution, each pore may be placed in a phase diagram (Fig. 5*A*). This phase diagram confirms a posteriori the most important feature of the problem treated in this paper: Both δ and ζ are of order 1, therefore none of them may be neglected. Both supersaturation and freezing must be taken into account to properly describe the pores. This justifies the complexity of Eq. **10**. It should be noted that removing

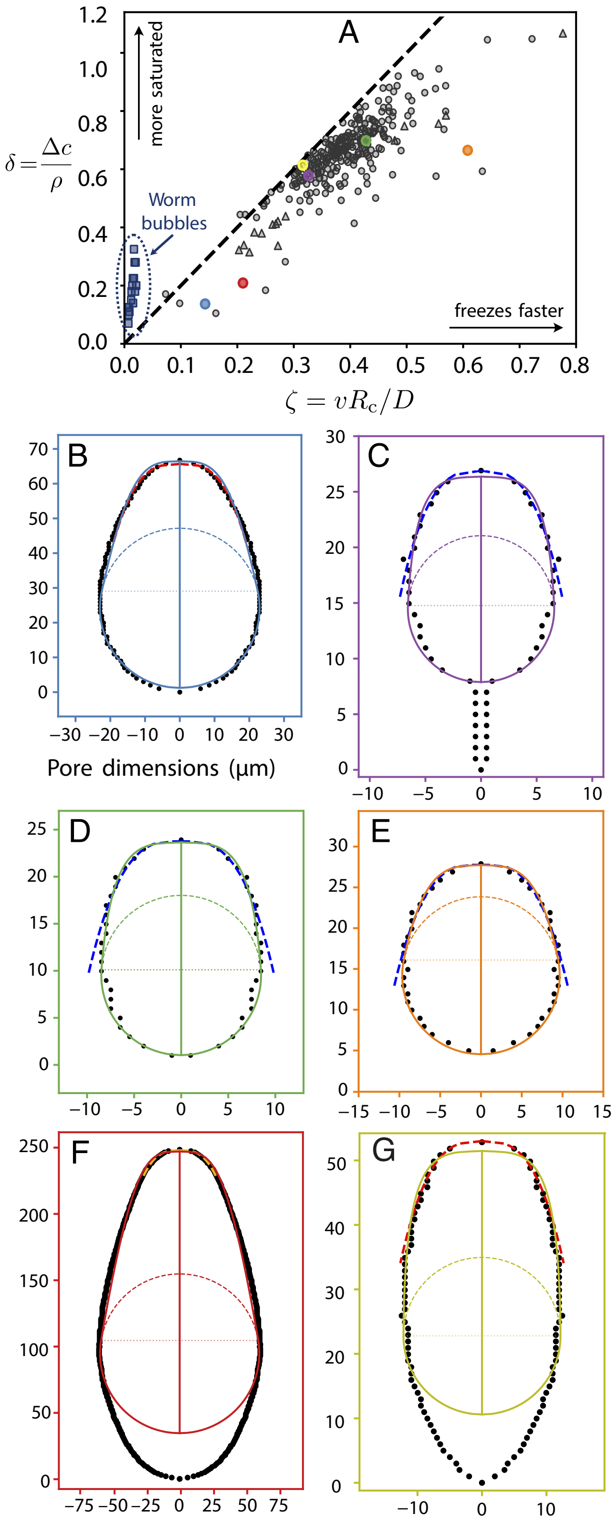

Fig. 5. (*A*) Phase diagram of the experiments. Each pore is represented by a point in the (ζ,δ) plane, with values obtained by matching a solution of the Frozen Bubble Equation (Eq. **13**) to its shape. Circles: first experimental system; triangles and squares: second system. Dark blue squares represent worm bubbles. The dashed line represents the critical value $\delta = 2\zeta$ above which the bifurcation to worm bubbles is predicted to occur. (*B*–*G*) Examples of shape matching, spanning the range of δ and ζ. The dashed circle represents the spherical initial condition. The thin dashed line inside the circle represents the initial condition R_0, Z_0 above which Eq. **13** is solved; the solid line represents the solution. The thick dashed line near the top of each profile shows the fit by the self-similar closing regime (Eq. **12**). Each sample is located in the phase diagram (*A*). All lengths are expressed in μm.

the transient diffusion term $\sqrt{\zeta/\pi Z}$ in Eq. **10** prevents from matching the shapes. Therefore, transient diffusion is important in the growth of the pore, contrary to recent assumptions (29). Nevertheless, this two-dimensional phase diagram is insufficient to characterize the pore shapes; two pores with similar δ and ζ but grown out of different initial conditions may have significantly different shapes (e.g. Fig. 5 *B* and *F* or *C* and *G*).

Most pores that we observe are well matched from *Top* to *Bottom*. Pores with a tail, due to nucleation between ice grains, are well matched starting above the tail (Fig. 5*C*). This suggests that transient gas diffusion following the nucleation is delayed until the bubble is free, and not stuck between ice grains. Some large pores can only be matched partially from some height Z_0 to their tip (Fig. 5 *F* and *G*). In these cases, the bottom of the pore does not have a uniform curvature, so our assumption that the bubble is left spherical by the entrapment probably fails. It is also likely that for very slow freezing, wetting effects become noticeable and our assumption of a hemispherical bubble fails as well.

In addition to matching the full solution of the Frozen Bubble Equation, we also fit the self-similar regime corresponding to the closing of the pore (Eq. **12**). In each of Fig. 5 *B*–*G*, a thick dashed line with a contrasting color shows the good agreement between the various experimental profiles and the scaling law $R \propto (Z_{\max} - Z)^{1/3}$. It should be noted that even in cases where we struggle to obtain a good match between the profile and the full solution (like Fig. 5*G*), the self-similar regime near the top is recovered.

Measurements. In the following, we consider pores frozen during a single experiment, corresponding to Fig. 1*C*. The large number of pores formed during the same experiment enables to study their statistics (*SI Appendix*). These pores were frozen at a freezing rate 133 μm/s ± 10 μm/s; in Fig. 5*A* they are situated in the main cloud of points. Matching a solution of the Frozen Bubble Equation to each pore, we can measure its nucleation radius; $R_c = 5.8\ \mu\text{m} \pm 0.7\ \mu\text{m}$. From the definition of R_c follows the supersaturation: $\Delta c = 0.76 \pm 0.1$ g/L, which is more than 40-fold the initial concentration (*Materials and Methods*).

Shape matching enables to measure R_0 and Z_0 for each bubble; we find $R_0 = 7.8\ \mu\text{m} \pm 1\ \mu\text{m}$ and $Z_0 = 8.2\ \mu\text{m} \pm 1.4\ \mu\text{m}$. These values close to the nucleation radius show that entrapment occurs very shortly after nucleation. The initial condition R_0 and Z_0 corresponds to some time T_0 after the bubble nucleation. $T_0 = Z_0/v$ is the delay between the nucleation (when $R = 0$) and the point at which $R = R_0$. We measure $T_0 = 60$ ms $\pm\ 12$ ms.

In order to obtain a simple form for the Frozen Bubble Equation, we have assumed that the bubble meets the freezing front with a right angle; in reality, this angle is $\pi/2 + \varepsilon$ and we have neglected ε. Shape matching enables to measure the initial slope R_0' that the bubble makes with the freezing front and that we assumed to be zero to simplify the description of diffusion. We find that $R_0' = -0.06 \pm 0.04$, corresponding to angle $\varepsilon_0 = -\arctan R_0' = 3.4 \pm 2.3^\circ$, which is indeed negligible.

Another remarkable result concerns the ratio R_0/R_c, which is the actual initial condition in the nondimensional Eq. **10**. Its value is $1.33 \pm 3 \times 10^{-4}$, which is an extremely narrow range. This is likely due to the conditions in which the bubble nucleates at the freezing front. A very narrow range of values suggests that the nucleation crevices (45) have very similar sizes and shapes in the given range of freezing rate. More analysis is required to describe these results quantitatively.

Worm Bubbles. Shape matching can also be applied to worm bubbles. In Fig. 6, we use this technique to measure δ, ζ, and R_c for various worm bubbles, as well as their equilibrium radius R_∞ (Fig. 6*B*), during or after their growth. For the latter, we neglect the closed tips that occur due to the above-mentioned fluctuations. According to Eqs. **14** and **15**, worm bubbles occur when two conditions are fulfilled: $\delta > 2\zeta$ and $R_0/R_c > R_-$. In this case, the stable radius of the worm bubble is equal to R_+. Placing our measurements on a phase diagram for the bifurcation (Fig. 6*C*) confirms that our model accurately predicts when worm bubbles appear as well as their equilibrium radius.

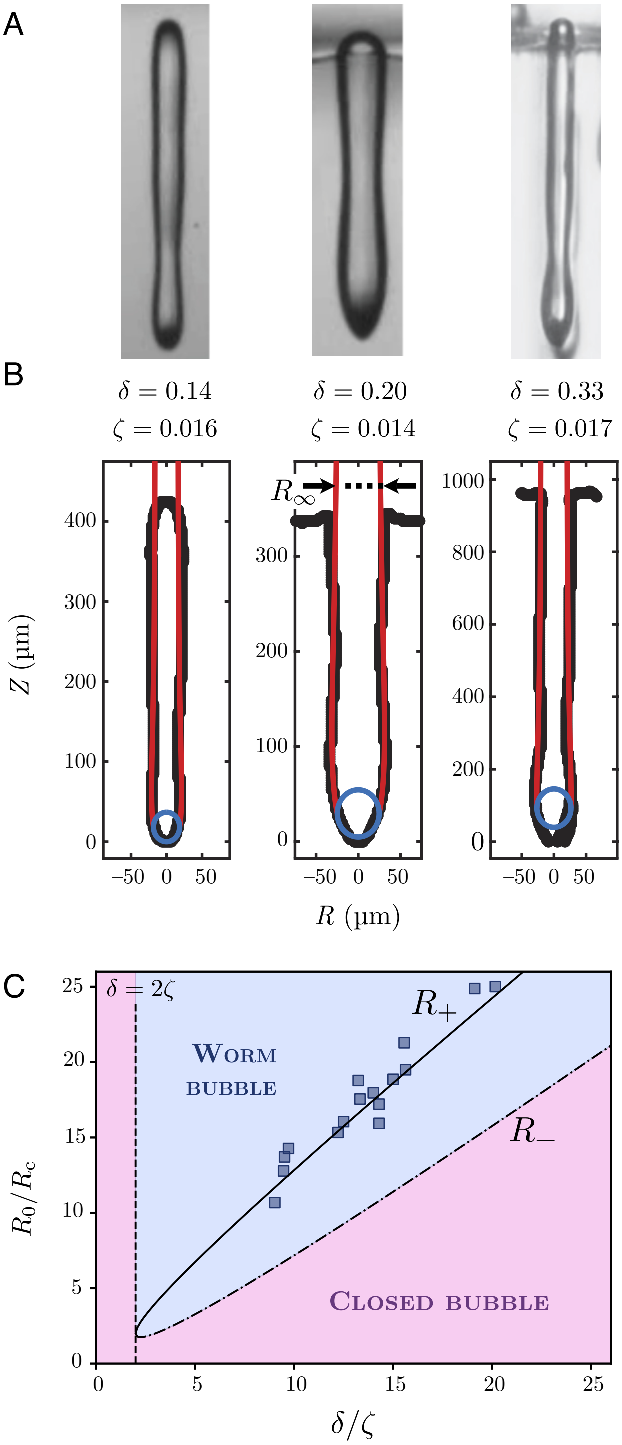

Fig. 6. (*A*) Pictures of various worm bubbles with (*B*) their shapes matched (solution in red, initial condition in blue). (*C*) Phase diagram predicting whether the bubble will close (purple) or not (blue), depending on parameters δ and ζ and on the initial condition R_0. The equilibrium radius of worm bubbles R_∞ must be equal to R_+ (Eq. **15**). Dark blue squares show the experimental measurements of R_∞.

Conclusion

The shape of gas bubbles trapped in ice results of simultaneous freezing and growth by gas diffusion. Heat transfer and capillarity set the shape of the bubble and of the freezing front. Depending on the bubble size relative to the nucleation radius R_c, diffusion makes it grow or shrink.

We have demonstrated that the shapes of bubbles trapped in ice, although extensively diverse, can be accurately described by a single nonlinear ordinary differential equation, the Frozen Bubble Equation (Eq. **10**). The nondimensional parameters δ and ζ, respectively representing the supersaturation and the freezing velocity, suffice to describe the growth of a bubble from a given initial condition $R_0 = R(Z_0)$. The asymptotic regimes explain why the tip of the pores is so characteristically rounded—it follows a power law (Eq. **12**)—and why the quickly frozen bubbles tend to be slightly elongated—the limit shape absent diffusion is a cone. Matching a solution of the Frozen Bubble Equation to the shape of a real pore enables to measure the supersaturation and the nucleation radius at which the pore appeared. We have shown that this is at least possible for freezing rates in the range 12 µm/s to 263 µm/s.

The mathematical analysis reveals a bifurcation that explains how worm bubbles, these cylindrical pores of potentially several centimeters, are formed. It yields the conditions for worm bubbles to appear as well as their equilibrium radius. Both are confirmed by our experiments. In further work, it would be interesting to validate the model against measurements made using different gases, with different solubility, such as CO_2 (higher solubility) or argon (lower solubility), and in a wider range of freezing rates.

Our model is written in the most parsimonious fashion; it describes the pores well with as few parameters and mechanisms as possible. It could be extended to take into account the impact of neighbor bubbles on the concentration field (46). Mathematical analysis could also be extended to the case in which the freezing rate is not constant but decreases as the freezing front moves away from the thermostat (47). Our work is applicable to measuring the freezing history of porous ice. It could also be used to help the design of porous freeze-cast materials.

Materials and Methods

Solution. We use deionized water left in contact with air for a few days so that gases dissolve in it. Before the experiment, the concentration of oxygen in the water was measured at $c_{O_2} = 6.7$ mg/L at 21 °C. Using known correlations of the solubility and Henry constant with the temperature (42), we obtain the concentration of nitrogen $c_{N_2} = 11.6$ mg/L, and the concentration of air as a mixture of both gases $c_0 = 18.3$ mg/L. We do not take into account further differences between oxygen and nitrogen.

Experiments. Our experiments consist in freezing water contained in a Hele-Shaw cell (Fig. 1*A*). We have used two separate experimental setups.

In the main setup, we used glass capillary tubes of rectangular section (Vitrocom), with inner dimensions 6 mm by 300 µm for the bigger cell, 2 mm by 100 µm for the smaller cell. No significant effect on the bubble shape of using one or the other cell was found. The freezing of the water column is recorded with is recorded with a camera (Nikon D5600) mounted with a macrolens (Nikon

Micro-Nikkor AI-s 200 mm f/4) and a microscope lens (Mitutoyo). The whole set-up is backlit by a light panel (Phlox). The capillary is first filled up with water and then carefully brought in contact with a thermostat, whose temperature is kept constant at −25 °C throughout the experiment. The thermostat is a hollow copper plate through which cold oil is pumped from a refrigerating bath (Julabo Corio 1000F). The local rate of freezing is set by the rate at which the latent heat released at the ice–water interface diffuses through the ice to the thermostat (47). Therefore, for a given heat flux absorbed by the thermostat, v decreases with the distance to the thermostat and with the section of the Hele-Shaw cell. We measure the local rate of freezing v on each video, next to each bubble. For all the experiments that we discuss in the present paper, v remains constant (within a few μm/s) during the formation of each bubble; it ranges from 12 to 263 μm/s.

The second experimental setup, used to study the formation of worm bubbles, follows a similar design and protocol (*SI Appendix*). In short, room temperature water is deposited between two acrylic plates (spaced 1 mm apart) on a cooled and frosted substrate, which is mounted on top of a freezing stage (BFS-40 MPA, Physitemp). The temperature of the substrate at the base of the deposited water is measured by a thermocouple. By varying the temperature of the substrate we control the range of freezing velocities, here limiting ourselves to a substrate temperature of −7.5 °C, yielding velocities between 4 μm/s to 17 μm/s, ensuring the formation of worm bubbles. The freezing process is recorded in side-view using a camera (Nikon D850) connected to a long working distance lens (Thorlabs, MVL12X12Z). The sample is illuminated with a diffused cold-white light-emitting diode to avoid local heating.

Numerical Resolution. The Frozen Bubble Equation was integrated using a fourth-order Runge–Kutta scheme in a custom Python routine.

Compressibility Effects. In the derivation, we have assumed that air has constant density. Compressibility can be taken into account when we develop the time derivative of the mass in Eq. **7**, by introducing the isothermal compressibility $\chi = \rho^{-1}\left(\partial\rho/\partial P\right)$. The calculation yields a slightly different version of Eq. **10**:

$$\frac{\mathrm{d}R}{\mathrm{d}Z} = \delta\left(\frac{R-1}{R-\frac{R_\chi}{R_\mathrm{c}}}\right)\left(\frac{1}{R}+\sqrt{\frac{\zeta}{\pi Z}}\right)-\frac{1}{2}, \qquad [16]$$

where $R_\chi = 2\gamma\chi/3$ is the length scale associated to compressibility. The first term of Eq. **16** resembles equation 6 of ref. 6, which follows from a different derivation that starts from the equation of state of the gas. In the limit $R_\chi \ll R_\mathrm{c}$ Eq. **10** is recovered. For air $\chi \simeq 10^{-5}$ Pa^{-1}, so $R_\chi \simeq 0.5$ μm. In our experiments R_c is at least ten times larger, therefore compressibility is negligible compared to dissolution.

Data, Materials, and Software Availability. All study data are included in the article and/or supporting information.

ACKNOWLEDGMENTS. This material is based upon work supported by the NSF under NSF Faculty Early Career Development (CAREER) Program Award CBET No. 1944844, and by a University of California, Santa Barbara Senate Faculty Grant. V.T. and A.S. thank Sylvain Deville and Cécile Monteux for fruitful discussions at the early stages of the project, and Sylvain Deville especially for reviewing the first version of the manuscript. V.T. warmly thanks Laurent Duchemin for insightful discussions about the mathematical methods. J.G.M. and D.L. thank the Balzan Foundation for support.

1. S. G. Warren, Optical properties of ice and snow. *Philos. Trans. R. Soc. A* **377**, 20180161 (2019).
2. K. Murakami, H. Nakajima, Formation of pores during unidirectional solidification of water containing carbon dioxide. *Mater. Trans.* **43**, 2582–2588 (2002).
3. B. Chalmers, How water freezes. *Sci. Am.* **200**, 114–123 (1959).
4. G. K. Swinzow, *Ice Cover of an Arctic Proglacial Lake* (US Army Materiel Command, Cold Regions Research & Engineering Laboratory, 1966), vol. 155.
5. P. Wei, C. Huang, K. Lee, Nucleation of bubbles on a solidification front–experiment and analysis. *Metall. Mater. Trans. B* **34**, 321–332 (2003).
6. S. Bari, J. Hallett, Nucleation and growth of bubbles at an ice-water interface. *J. Glaciol.* **13**, 489–520 (1974).
7. A. J. Gow, D. Langston, *Growth History of Lake Ice in Relation to its Stratigraphic, Crystalline and Mechanical Structure* (Department of Defense, Army Corps of Engineers, Cold Regions Research, 1977), vol. 77.
8. M. E. Wengrove, E. C. Pettit, J. D. Nash, R. H. Jackson, E. D. Skyllingstad, Melting of glacier ice enhanced by bursting air bubbles. *Nat. Geosci.* **16**, 871–876 (2023).
9. K. Charra-Vaskou *et al.*, Xylem embolism and bubble formation during freezing suggest complex dynamics of pressure in betula pendula stems. *J. Exp. Bot.* **74**, 5840–5853 (2023).
10. S. Ghosh, J. N. Coupland, Factors affecting the freeze-thaw stability of emulsions. *Food Hydrocoll.* **22**, 105–111 (2008).
11. C. Körber, Phenomena at the advancing ice-liquid interface: Solutes, particles and biological cells. *Q. Rev. Biophys.* **21**, 229–298 (1988).
12. G. Kletetschka, J. Hruba, Dissolved gases and ice fracturing during the freezing of a multicellular organism: Lessons from tardigrades. *BioRes. Open Access* **4**, 209–217 (2015).
13. V. Shapovalov, L. Boyko, Gasar–a new class of porous materials. *Adv. Eng. Mater.* **6**, 407–410 (2004).
14. T. Yokokawa, Gas solubilities in molten salts and silicates. *Pure Appl. Chem.* **58**, 1547–1552 (1986).
15. O. Bunoiu, T. Duffar, I. Nicoara, Gas bubbles in shaped sapphire. *Prog. Cryst. Growth Charact. Mater.* **56**, 123–145 (2010).
16. E. Ghezal, A. Nehari, K. Lebbou, T. Duffar, Observation of gas bubble incorporation during micropulling-down growth of sapphire. *Cryst. Growth Des.* **12**, 5715–5719 (2012).
17. A. Gupta, B. Saxena, S. Tiwari, S. Malhotra, Pore formation in cast metals and alloys. *J. Mater. Sci.* **27**, 853–862 (1992).
18. M. V. Bianchi, R. Viskanta, Gas segregation during solidification processes. *Int. J. Heat Mass Transf.* **40**, 2035–2043 (1997).
19. H. Nakajima, S. Hyun, K. Ohashi, K. Ota, K. Murakami, Fabrication of porous copper by unidirectional solidification under hydrogen and its properties. *Colloids Surf. A Physicochem. Eng. Asp.* **179**, 209–214 (2001).
20. S. Deville, E. Saiz, R. K. Nalla, A. P. Tomsia, Freezing as a path to build complex composites. *Science* **311**, 515–518 (2006).
21. S. Deville, E. Saiz, A. P. Tomsia, Ice-templated porous alumina structures. *Acta Mater.* **55**, 1965–1974 (2007).
22. S. Deville, Freeze-casting of porous ceramics: A review of current achievements and issues. *Adv. Eng. Mater.* **10**, 155–169 (2008).
23. S. Deville, Freeze-casting of porous biomaterials: Structure, properties and opportunities. *Materials* **3**, 1913–1927 (2010).
24. D. R. Uhlmann, B. Chalmers, K. Jackson, Interaction between particles and a solid-liquid interface. *J. Appl. Phys.* **35**, 2986–2993 (1964).
25. R. Asthana, S. Tewari, The engulfment of foreign particles by a freezing interface. *J. Mater. Sci.* **28**, 5414–5425 (1993).
26. S. Tyagi, H. Huynh, C. Monteux, S. Deville, Objects interacting with solidification fronts: Thermal and solute effects. *Materialia* **12**, 100802 (2020).
27. S. Tyagi, C. Monteux, S. Deville, Solute effects on the dynamics and deformation of emulsion droplets during freezing. *Soft Matter* **18**, 4178–4188 (2022).
28. J. G. Meijer, P. Kant, D. Van Buuren, D. Lohse, Thin-film-mediated deformation of droplet during cryopreservation. *Phys. Rev. Lett.* **130**, 214002 (2023).
29. K. Shao, M. Song, X. Zhang, L. Zhang, Growth and distribution characteristics of trapped air bubbles in ice slices. *Phys. Fluids* **35**, 113319 (2023).
30. P. Wei, Y. Kuo, S. Chiu, C. Ho, Shape of a pore trapped in solid during solidification. *Int. J. Heat Mass Transf.* **43**, 263–280 (2000).
31. P. Wei, S. Hsiao, Effects of solidification rate on pore shape in solid. *Int. J. Therm. Sci.* **115**, 79–88 (2017).
32. D. Anderson, M. G. Worster, S. Davis, The case for a dynamic contact angle in containerless solidification. *J. Cryst. Growth* **163**, 329–338 (1996).
33. J. H. Snoeijer, P. Brunet, Pointy ice-drops: How water freezes into a singular shape. *Am. J. Phys.* **80**, 764–771 (2012).
34. A. Marín, O. Enríquez, P. Brunet, P. Colinet, J. Snoeijer, Universality of tip singularity formation in freezing water drops. *Phys. Rev. Lett.* **113**, 054301 (2014).
35. L. Seguy, S. Protière, A. Huerre, Role of geometry and adhesion in droplet freezing dynamics. *Phys. Rev. Fluids* **8**, 033601 (2023).
36. C. A. Knight, The contact angle of water on ice. *J. Colloid Interface Sci.* **25**, 280–284 (1967).
37. V. Thiévenaz, C. Josserand, T. Séon, Retraction and freezing of a water film on ice. *Phys. Rev. Fluids* **5**, 041601(R) (2020).
38. A. Huerre, A. Monier, T. Séon, C. Josserand, Solidification of a rivulet: Shape and temperature fields. *J. Fluid Mech. Res.* **914**, A32 (2021).
39. P. Wei, C. Huang, Z. Wang, K. Chen, C. Lin, Growths of bubble/pore sizes in solid during solidification–an in situ measurement and analysis. *J. Cryst. Growth* **270**, 662–673 (2004).
40. J. G. Meijer, D. Rocha, A. M. Linnenbank, C. Diddens, D. Lohse, Enhanced bubble growth near an advancing solidification front. *J. Fluid Mech. Res.* **996**, A22 (2024).
41. S. Lubetkin, The fundamentals of bubble evolution. *Chem. Soc. Rev.* **24**, 243–250 (1995).
42. D. R. Lide *et al.*, *CRC Handbook of Chemistry and Physics* (CRC Boca Raton, 2012).
43. P. S. Epstein, M. S. Plesset, On the stability of gas bubbles in liquid-gas solutions. *J. Chem. Phys.* **18**, 1505–1509 (1950).
44. V. Arnold, *Ordinary Differential Equations* (Springer Science & Business Media, 1992).
45. A. A. Atchley, A. Prosperetti, The crevice model of bubble nucleation. *J. Acoust. Soc. Am.* **86**, 1065–1084 (1989).
46. K. Yoshimura, T. Inada, S. Koyama, Growth of spherical and cylindrical oxygen bubbles at an ice-water interface. *Cryst. Growth Des.* **8**, 2108–2115 (2008).
47. V. Thiévenaz, T. Séon, C. Josserand, Solidification dynamics of an impacted drop. *J. Fluid Mech. Res.* **874**, 756–773 (2019).